



SPITZER OBSERVATIONS CONFIRM AND RESCUE THE HABITABLE-ZONE SUPER-EARTH K2-18b FOR FUTURE CHARACTERIZATION

BJÖRN BENNEKE¹, MICHAEL WERNER², ERIK PETIGURA¹, HEATHER KNUTSON¹, COURTNEY DRESSING^{1,9}, IAN J. M. CROSSFIELD^{3,4,9}, JOSHUA E. SCHLIEDER⁵, JOHN LIVINGSTON², CHARLES BEICHMAN⁶, JESSIE CHRISTIANSEN⁷, JESSICA KRICK⁷, VAROUJAN GORJIAN², ANDREW W. HOWARD⁸, EVAN SINUKOFF⁸, DAVID R. CIARDI⁶, AND RACHEL L. AKESON⁷

¹ Division of Geological and Planetary Sciences, California Institute of Technology, Pasadena, CA 91125, USA; bbenneke@caltech.edu

² Jet Propulsion Laboratory, California Institute of Technology, USA

³ Department of Astronomy and Astrophysics, University of California, Santa Cruz, CA 95064, USA

⁴ Lunar & Planetary Laboratory, University of Arizona, 1629 E. University Blvd., Tucson, AZ, USA

⁵ NASA Ames Research Center, Moffett Field, CA, USA

⁶ NASA Exoplanet Science Institute, California Institute of Technology, 770 S. Wilson Ave., Pasadena, CA, USA

⁷ Infrared Processing and Analysis Center, California Institute of Technology, Pasadena, CA 91125, USA

⁸ Institute for Astronomy, University of Hawaii, 2680 Woodlawn Drive, Honolulu, HI, USA

Received 2016 January 25; revised 2016 September 17; accepted 2016 October 23; published 2017 January 12

ABSTRACT

The recent detections of two transit events attributed to the super-Earth candidate K2-18b have provided the unprecedented prospect of spectroscopically studying a habitable-zone planet outside the solar system. Orbiting a nearby M2.5 dwarf and receiving virtually the same stellar insolation as Earth, K2-18b would be a prime candidate for the first detailed atmospheric characterization of a habitable-zone exoplanet using the *Hubble Space Telescope* (*HST*) and *James Webb Space Telescope* (*JWST*). Here, we report the detection of a third transit of K2-18b near the predicted transit time using the *Spitzer Space Telescope*. The *Spitzer* detection demonstrates the periodic nature of the two transit events discovered by *K2*, confirming that K2-18 is indeed orbited by a super-Earth in a 33 day orbit, ruling out the alternative scenario of two similarly sized, long-period planets transiting only once within the 75 day *Kepler Space Telescope* (*K2*) observation. We also find, however, that the transit event detected by *Spitzer* occurred 1.85 hr (7σ) before the predicted transit time. Our joint analysis of the *Spitzer* and *K2* photometry reveals that this early occurrence of the transit is not caused by transit timing variations, but the result of an inaccurate ephemeris due to a previously undetected data anomaly in the *K2* photometry. We refit the ephemeris and find that K2-18b would have been lost for future atmospheric characterizations with *HST* and *JWST* if we had not secured its ephemeris shortly after the discovery. We caution that immediate follow-up observations as presented here will also be critical for confirming and securing future planets discovered by the Transiting Exoplanet Survey Satellite (*TESS*), in particular if only two transit events are covered by the relatively short 27-day *TESS* campaigns.

Key words: astrobiology – planets and satellites: detection – planets and satellites: individual (K2-18b) – techniques: photometric

1. INTRODUCTION

Ever since the discovery of the first planet orbiting a Sun-like star, we have made steady progress toward finding habitable-zone exoplanets with the eventual goal to characterize their atmospheres and climates in great detail. Results from the *Kepler* mission, which was the first telescope with the sensitivity to detect small planets in the habitable zones of Sun-like stars, indicate that the occurrence rate for habitable Earths (“ η_{\oplus} ”) may be as high as 5%–20% (Petigura et al. 2013; Foreman-Mackey et al. 2014; Burke et al. 2015; Silburt et al. 2015; Farr et al. 2015). The majority of these planets found from the *Kepler* mission, however, are orbiting distant and faint stars, preventing us from measuring their bulk masses or atmospheric compositions through spectroscopy.

The recent announcement of the super-Earth candidate K2-18b (Montet et al. 2015) orbiting in the habitable zone of a nearby bright M2.8-dwarf provides the unprecedented opportunity to characterize the first atmosphere of a habitable zone planet outside our solar system. Atmospheric studies of K2-18b are within the reach of currently available instrumentation because the radius of the host star K2-18 is only $0.39 R_{\odot}$ and the planet’s radius of $2.2 R_{\oplus}$ allows for the presence of a

hydrogen-rich, low mean molecular weight gas envelope. Water and methane absorption in such a hydrogen-rich atmosphere could result in transit depth variations that can be revealed through *Hubble Space Telescope* (*HST*), *Spitzer*, and/or *James Webb Space Telescope* (*JWST*) transit observations.

The two transit events of the planet candidate K2-18b were originally discovered by analyzing the Campaign 1 data from the extended *Kepler Space Telescope* (“*K2*”) mission (Foreman-Mackey et al. 2015). Modern seeing-limited images and adaptive optics imaging subsequently ruled out background eclipsing binaries as a possible source for the detected transit events (Montet et al. 2015). Radial velocity measurements further eliminated the possibility that the apparent transit events were caused by non-planetary companions co-moving with K2-18b.

The *K2* photometry, however, could not demonstrate the periodic nature of the transit signal. Instead, the 80 day *K2* photometry identified only two transit events of similar depth with a separation of 33 days. Meanwhile, radial velocity confirmation of the 33 day period is currently not available because the host star is faint at visible wavelengths ($V = 13.5$) and the expected semi-amplitude of a 33 day period planet would only be $K_S = 1\text{--}2 \text{ m s}^{-1}$. As a result, the available observations leave open the alternative scenario that the two

⁹ NASA Sagan Fellow.

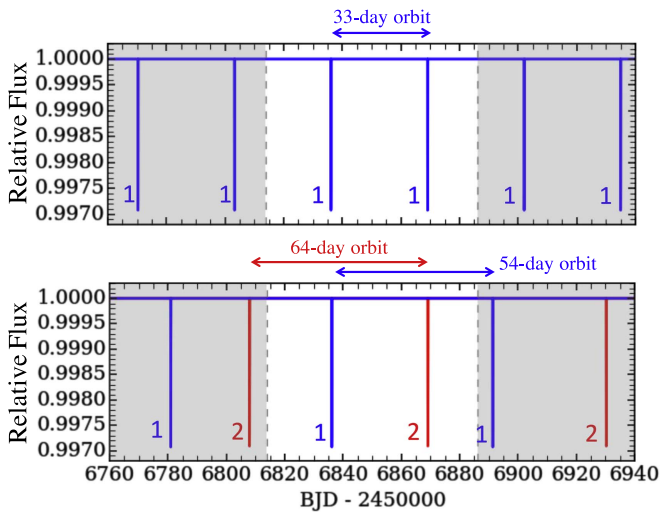


Figure 1. Plausible scenarios in agreement with the available *K2* data of K2-18. The white region indicates the time span observed by *K2*. The two detected transit events at BJD = 2, 456, 836 and BJD = 2, 456, 869 can be fit equally well by a single planet in a 33 day orbit at low impact parameter (top panel) or two long-period planets at slightly higher impact parameter (bottom panel).

detected transit events on 2014 June 27 and 2014 July 30 were caused by two similarly sized, long-period planets ($\gtrsim 50$ days) that happen to transit only once within the 80 days observation in *K2* Campaign 1 (Figure 1). In this two-planet scenario, a planet with a 33 day orbital period and Earth-like incident stellar irradiance ($S_{\text{inc}} \approx S_{\oplus}$) would not exist around the star K2-18. We find that two-planet scenarios can lead to equally good fits to the long-cadence *K2* data because the increase in transit duration with orbital period can effectively be compensated by a high impact parameter and/or an eccentric orbit.

To distinguish between the one and two planet scenario, we obtained *Spitzer* high precision photometry at $4.5 \mu\text{m}$ to probe for a third transit event that would only occur if a habitable-zone super-Earth indeed existed in a 33 day orbit around K2-18. A detection of a third transit at the predicted time would prove the periodic nature of the signal. It would simultaneously also rule out potential scenarios in which one or both of the identified transit-like events were the result of residual systematic effects in the corrected *K2* photometry. Such scenarios are conceivable because the detected signals are well below the noise floor of the uncorrected *K2* photometry and outliers well above the median light curve scatter are common in the corrected *K2* photometry despite state-of-the-art detrending (e.g., Vanderburg & Johnson 2014; Foreman-Mackey et al. 2015).

The article is structured as follows. In Section 2, we describe the *Spitzer* and *K2* observations used in this work as well as our photometric extraction routines. Section 3 presents the light curves analyses. Finally, we discuss the results and conclusions in Section 4.

2. OBSERVATIONS

2.1. *Spitzer*/IRAC

We observed the star K2-18 (EPIC 201912552) for a total of 8.1 hr on 2015 August 29 to search for the predicted transit of the super-Earth candidate K2-18b as part of our *K2* follow-up program (GO 11026, PI Werner, see also Beichman

et al. 2016). The science observation began three hours before the start of the predicted transit of K2-18b and ended two hours after the end of the predicted transit to account for transit ephemeris uncertainties and to provide adequate baselines on either side of the transit. An additional 30 minute of pre-observation (not used in the analysis) preceded the science observation to mitigate the initial instrument drift in the science observations resulting from telescope temperature changes after slewing from the preceding target (Grillmair et al. 2012). Both pre-observation and science observations were taken using *Spitzer*/IRAC Channel 2 in stare mode. To enhance the accuracy in positioning the target star K2-18 on the IRAC detector, the pre-observations were taken in peak-up mode using the Pointing Calibration and Reference Sensor as a positional reference.

We chose *Spitzer*/IRAC Channel 2 ($4.5 \mu\text{m}$) because the instrumental systematic due to intra-pixel sensitivity variations are smaller for Channel 2 than for Channel 1 (Ingalls et al. 2012). Our exposure times were set to 2 s to optimize the integration efficiency while comfortably remaining in the linear regime of the IRAC detector. Subarray mode was used to reduce the readout overhead and lower the data volume for the downlink. In total, our science data are composed of 13,632 individual frames forming a 7.6 hr broadband photometric time series of K2-18 at $4.5 \mu\text{m}$.

We extract multiple photometric light curves from the science data using a wide range of fixed and variable aperture sizes. The purpose of extracting and comparing multiple photometric light curves is to choose the aperture that provides the lowest residual scatter and red-noise component. For each aperture, our extraction includes estimating and subtracting the sky background, calculating the flux-weighted centroid position of the star on the array, and then calculating the total flux within circular apertures (Knutson et al. 2012; Lewis et al. 2013; Todorov et al. 2013; Kammer et al. 2015). For the fixed apertures we consider radii between 2.0 and 5.0 pixels. For the time varying apertures, we first calculate the scaling of the noise pixel parameter $\beta = (\sum_n I_n)^2 / (\sum_n I_n^2)$, where I_n is the measured intensity in the n th pixel (Mighell 2005), and then iteratively rescale the noise pixel aperture radius as $r = a\sqrt{\beta} + c$, where we explore values between 0.6 and 1.2 for the scaling factors a and values between 0.6 and 1.2 for the constant c . We choose this range for a and c because we noted in previous *Spitzer* work that the photometric scatter increases outside this range (Kammer et al. 2015). Finally, we pick the version of the *Spitzer* photometry with the lowest red-noise component. Our red-noise measure is the summed square difference between the noise scaling obtained by successively doubling the bin size and the theoretical square-root noise scaling for a Poisson process (Figure 2). In our case, the version of the photometry with the lowest red-noise also results in the lowest rms.

Our analysis is performed on the entire 7.6 hr science data since there is no evidence for a residual ramp effect at the beginning of the science data. We normalize the light curve by the median value and bin the data to 60 s cadence. We find that moderate binning to 60 s does not affect the information content of the photometry, but provides more signal per data point allowing an improved correction of the systematics (Section 3). We calculate BJD_{UTC} mid-exposure times using the information in the header of the BCD files provided by the *Spitzer* pipeline. We show the resulting uncorrected light curve

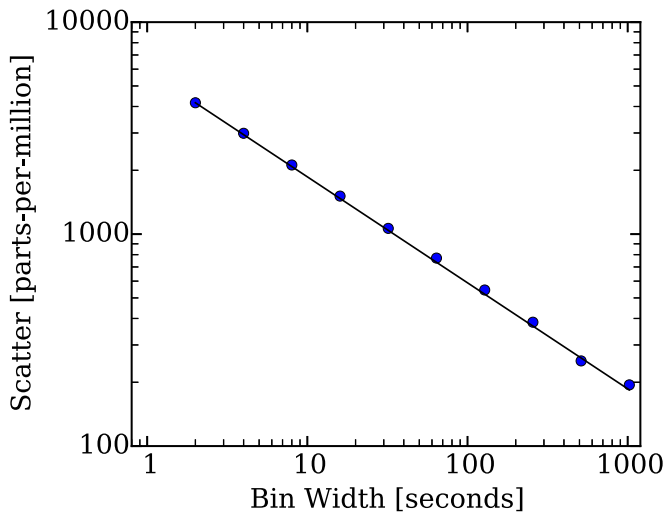


Figure 2. Photometric scatter vs. the width of the binning interval for *Spitzer* data of K2-18b. The root-mean-square error of the systematics-corrected *Spitzer* data (blue points) follows closely the theoretical square-root scaling for uncorrelated white noise (black line). The left-most data point corresponds to the unbinned 2 s exposures.

for the fixed aperture with a radius of 3.0 pixels in Figure 3 (bottom panel).

2.2. K2 Photometry

The star K2-18 was observed by the *Kepler Space Telescope* as part of K2 Campaign 1 covering an 80 day time span between 2014 November 14 and 2015 February 3. We extract the K2 photometry directly from the *Kepler* pixel data downloaded from the Mikulski Archive for Space Telescopes. The star is listed as EPIC-201912552. The full data set is a time series composed of 3737 individual 16×16 pixel images centered on the star K2-18. The individual images have a cadence of 29.4 minute and were obtained by co-adding 270 exposures (each 6.02 s plus 0.52 s readout) onboard the *Kepler* spacecraft (Gilliland et al. 2010). We do not do any additional time binning during the photometric extraction and light curve analysis of the K2 data.

2.2.1. Photometric Extraction

Our photometric extraction routine is outlined in Crossfield et al. (2015) and Petigura et al. (2015), following the approach introduced by Vanderburg & Johnson (2014). In brief, during the continuous 80 day K2 observations, the stars drift across the CCD by approximately 1 pixel every 6 hr due to the spacecraft’s pointing jitter. As the stars drift through pixel-phase, intra-pixel sensitivity variations and errors in the flatfield cause the apparent brightness of the target star to change. We detrend the apparent brightness variations of our target using the telescope roll angle between the target frame and an arbitrary reference observation. For each of the two transits, we then extract transit light curves ranging from three hours before the transit ingress to three hours after ingress, providing sufficient baseline for the transit light curve analysis.

2.2.2. A Cosmic Ray Detection Algorithm for K2 Photometry

As shown in this work, cosmic ray hits can substantially affect the astrophysical results derived from K2 photometry. This is particularly troubling because the effects of cosmic ray

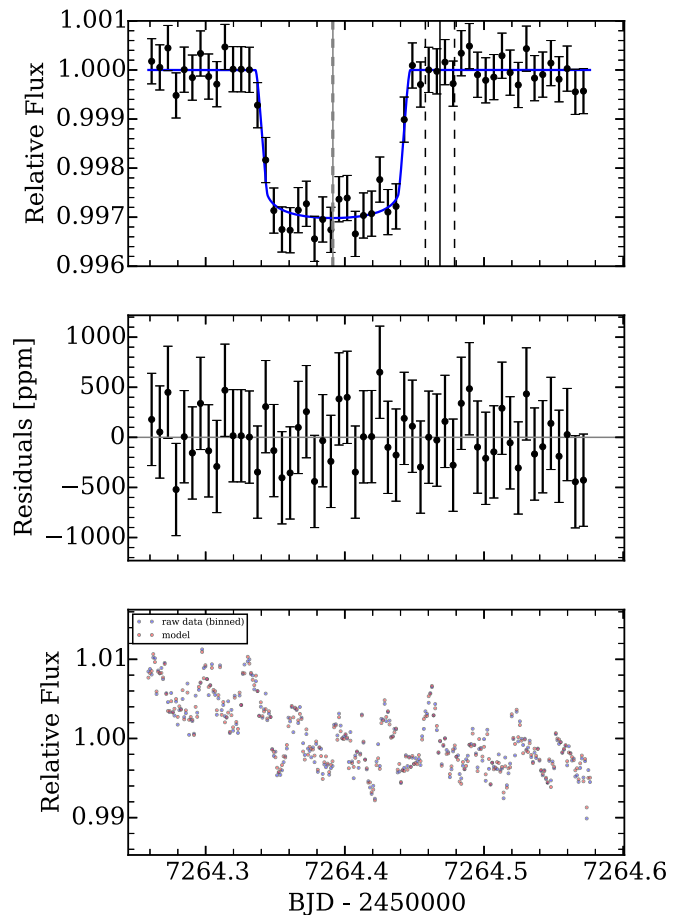


Figure 3. Light curve fit to the *Spitzer* transit observation of K2-18b. The top panel shows the best fitting model light curve (blue), overlaid with the systematics-corrected *Spitzer* data. The transit of K2-18b appears 7σ (1.85 hr) before the predicted transit time from Montet et al. (2015) (vertical black line). Residuals from the light curve fitting are plotted in the middle panel, with uncertainty bars corresponding to the fitted photometric scatter. The final systematics-corrected photometry is near the Poisson noise limit and virtually free of red noise and systematics. For clarity, *Spitzer* data are binned to 10 minute intervals. The bottom panel shows the raw *Spitzer* photometry (blue), overlaid with the model fit (red). Only *Spitzer* observations are used in this fit.

hits are generally too small to result in obvious outliers in the long-cadence, 30 minute K2 photometry. As a result, cosmic ray hits have stayed unnoticed to date, and at least for K2-18b have resulted in inaccurate estimates of the transit parameters. To address this issue and detect cosmic ray hits in the K2 photometry, we introduce a generally applicable algorithm to efficiently identify cosmic ray hits in the presence of substantial telescope jitter as we see for K2.

We apply the algorithm to the K2-18 data as follows. First, we remove the sky background from each individual frame by subtracting the median pixel value outside the point-spread function (PSF) of the target star. For each background-subtracted frame in the K2 image series, we then find a “most similar frame” by identifying the frame in the K2 image series that minimizes the weighted sum of the square differences in x and y centroid location and telescope roll angle. This most similar frame will generally appear virtually identical to the original frame because the PSF falls virtually identical on the detector pixels. The most similar frame can, therefore, be used to subtract the target star from the image and isolate potential

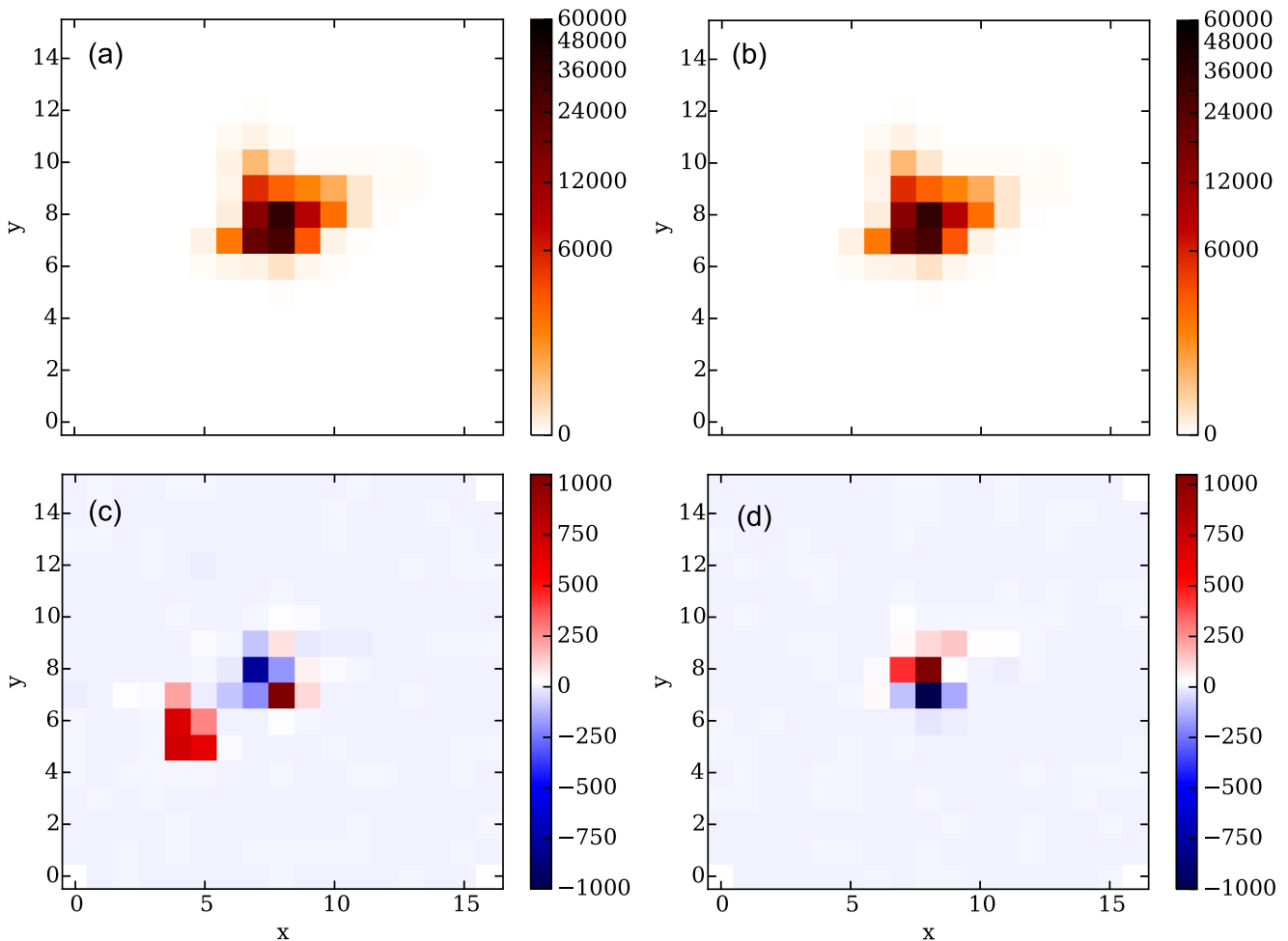


Figure 4. Cosmic ray detection for *K2* photometry. Panel (a) shows the background subtracted image of K2-18b for the observation affected by a cosmic ray hit (red data point in Figure 7). Panel (c) shows the same frame after subtracting the “most similar frame” in the *K2* time series of K2-18b (Panel (b)). The cosmic hit is clearly identified in the difference image near $x = 4.5$ and $y = 5.5$. For comparison, panel (d) shows an equivalent difference image for an observation not affected by a cosmic ray hit. Small residuals remain near the center of the PSF, but are not mistaken as cosmic ray hits by our new cosmic ray detection algorithm (Section 2.2.2)

cosmic ray hits. Finally, we automatically identify cosmic ray hits by searching for $>10\sigma$ outliers in the time series of each pixel in the difference images.

As an example, Figure 4 shows the detection of the cosmic ray hit near the ingress of the second *K2* transit observation of K2-18b. Panel (a) shows the background subtracted image of K2-18b for the cosmic-ray affected observation near the ingress of the second transit. For comparison, panel (b) shows the frame in the *K2*-18 data with the most similar centroid position (BJD = 2456875.66). Panels (a) and (b) appear virtually identical despite the strong color stretching. The cosmic ray hit near $x = 4.5$ and $y = 5.5$ becomes apparent, however, in the difference image (panel (c)). The five pixels near the cosmic ray hit are identified as outliers with a significance of $>20\sigma$ in the difference image light curves for these pixels. For comparison, panel (d) shows the difference image for a regular frame without a cosmic ray hit. Small residuals ($\sim 1\%$) in the difference image remain due to slight differences in the centroid position and shape of the PSF. However, the residuals are not mistaken as cosmic ray hits because the pixel values are within the variances of the difference image light curves for those pixels.

2.3. Stellar Spectroscopy

We observed K2-18 using the near-infrared cross-dispersed spectrograph (SpeX) on the NASA Infrared Telescope Facility (IRTF) to independently verify its metallicity ($[\text{Fe}/\text{H}]$), effective temperature ($T_{\text{eff},*}$), radius (R_*), mass (M_*), and luminosity (L_*). Following the procedure described in Crossfield et al. (2015), Petigura et al. (2015), and Schlieder et al. (2016), we obtain stellar properties that are consistent with the stellar properties reported by Montet et al. (2015) (Table 2). In short, we observed K2-18 using the short cross-dispersed mode and $0.3 \times 15''$ slit providing simultaneous wavelength coverage from 0.68 to $2.5 \mu\text{m}$ at a resolution of $R = 2000$ (Figure 5). The median signal-to-noise ratio (SNR) of our SpeX spectrum is 145 across the JHK bands. Based on the SpeX spectrum, we estimate the stellar metallicity using empirical methods based on the spectroscopic indices and equivalent widths calibrated using M dwarfs that have wide, co-moving FGK companions with well determined $[\text{Fe}/\text{H}]$ (Boyajian et al. 2012; Mann et al. 2013a). Similarly, we extract the effective temperature using temperature sensitive spectroscopic indices in the JHK bands (Mann et al. 2013b) and empirical relations calibrated using nearby, bright M dwarfs (Boyajian et al. 2012). We also

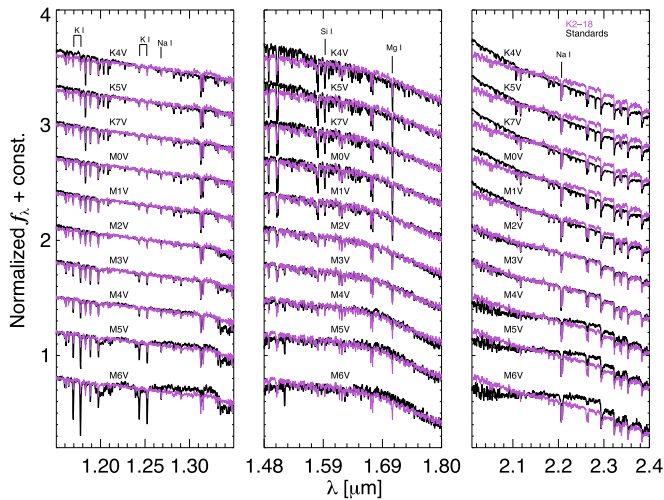


Figure 5. Calibrated IRTF/SpEx JHK-band spectrum of K2-18 compared to late-type standards from the IRTF Spectral Library. The spectra are normalized to the continuum in each band. Across the three bands, the continuum shape and the strengths of individual absorption features are most consistent with the M2/M3 standards. This is consistent with the $M2.5 \pm 0.5$ spectral type estimated using index based methods. Spectroscopically derived stellar parameters are listed in Table 2.

estimate the spectral type of K2-18 from our SpeX spectrum using the molecular index based methods of Lépine et al. (2013) (TiO_5 , CaH_3) and Rojas-Ayala et al. (2012) ($\text{H}_2\text{O} - \text{K}_2$). Both methods provide a spectral type of $M2.5 \pm 0.5$. This type is consistent with the derived stellar parameters and a visual comparison to late-type standards from the IRTF Spectral Library (Figure 5, Cushing et al. 2005; Rayner et al. 2009). Finally, we combine the derived $T_{\text{eff},*}$ and $[\text{Fe}/\text{H}]$ and compute the stellar radius and luminosity using the empirical $T_{\text{eff}} - [\text{Fe}/\text{H}] - R_*$ relation provided by Mann et al. (2015).

3. LIGHT CURVE ANALYSES

3.1. *Spitzer* Confirmation of K2-18b

We analyze the *Spitzer* raw photometry by simultaneously fitting our *Spitzer*/IRAC instrument model, a transit light curve model, and a photometric scatter parameter using Markov chain Monte Carlo (MCMC). The entire analysis from raw photometry to the transit parameters and their uncertainties is performed as a one-step, statistically consistent Bayesian analysis.

3.1.1. *Spitzer*/IRAC Instrument Model

Our *Spitzer*/IRAC instrument model accounts for intrapixel sensitivity variations and temporal sensitivity changes using a modified version of the systematics model proposed by Deming et al. (2015). Our instrument model is

$$S(t_i) = \frac{\sum_{k=1}^9 w_k D_k(t_i)}{\sum_{k=1}^9 D_k(t_i)} + m \cdot t_i, \quad (1)$$

where the sensitivity function $S(t_i)$ is composed of the pixel-level decorrelation (PLD) term introduced by Deming et al. (2015) and a linear sensitivity gradient in time. The $D_k(t_i)$'s in the PLD term are the raw counts in the 3×3 pixels, $k = 1 \dots 9$, covering the central region of the PSF. In the

numerator, these raw data values are multiplied by the nine time-independent PLD weights, $\{w_1 \dots w_9\}$, fitted as free parameters in the light curve analysis. Together with the linear slope m , the instrument model therefore includes 10 free instrument fitting parameters to capture the intrapixel sensitivity variations and temporal sensitivity changes. The differences between Equation (1) in this work and Equation (4) in Deming et al. (2015) are that we do not include the offset constant (h) and we apply $S(t_i)$ as a multiplicative correction factor corresponding to a variation in sensitivity rather than an additive term. The log-likelihood function for fitting the *Spitzer* raw photometry is then

$$\log L = -\frac{1}{2} \sum_{i=1}^N \left(\frac{D(t_i) - S(t_i) \cdot f(t_i)}{\sigma} \right)^2, \quad (2)$$

where $f(t_i)$ is the median-normalized flux summed over all pixels of the target's PSF, $S(t_i)$ is aforementioned instrument sensitivity, $f(t_i)$ is the model transit light curve, and σ is the photometric scatter parameter simultaneously fit with the instrument model and transit light curve parameters.

We do not include the constant term h from Deming et al. (2015) because only the relative sizes of the PLD weights carry information about the intrapixel sensitivity variation. The sum of the PLD weights $\sum_k w_k$ uniformly scales the entire light curve up or down, which is perfectly equivalent to adding a constant h . As a result, if an extra term h was included, it would be perfectly degenerate with $\sum_k w_k$ in the fitting, resulting in 100% degeneracies between the nine PLD weight and h .

We choose to include $S(t_i)$ as a multiplicative correction factor rather than an additive term as done by Deming et al. (2015) because the multiplicative factor matches more closely the underlying detector behavior, which is a variation in sensitivity (or quantum efficiency) across the pixel area. The difference between a multiplicative factor and an additive term is generally small because $S(t_i)$ is near unity and the multiplication can be approximated by $1 + \epsilon$. However, inaccuracy due to the negligence of the cross-term $\delta f \cdot \delta S$ can be as high as $0.01 \cdot 0.005 = 50$ parts-per-million for 1% transit depth and typical sensitivity variations. We choose to be on the safe side by introducing a multiplicative correction factor that correctly captures the cross-term $\delta f \cdot \delta S$.

3.1.2. Transit Model

We compute the transit light curve $f(t_i)$ using the *Batman* implementation (Kreidberg 2015) of the equations derived in Mandel & Agol (2002). The transit parameters fitted in our *Spitzer* analysis are the planet-to-star radius ratio R_p/R_* , the mid-transit time T_C , and the impact parameter b . We fix the stellar radius and mass to the values derived based on stellar spectroscopy (Table 2) and assume a circular orbit. We use a quadratic limb darkening profile with coefficients interpolated from the tables provided by Claret & Bloemen (2011) for K2-18's stellar effective temperature and surface gravity ($u_1 = 0.007 \pm 0.007$, $u_2 = -0.191 \pm 0.005$). These limb darkening coefficients are computed specifically for the $4.5 \mu\text{m}$ *Spitzer*/IRAC Channel 2 bandpass from spherically symmetric Phoenix models (e.g., Hauschildt et al. 1999) using updated opacities. We account for the ~ 30 minute cadence of the K2 observations by numerically integrating in time.

3.1.3. MCMC Analysis

We compute the joint posterior distribution of the instrument and transit parameters using the `emcee` package (Foreman-Mackey et al. 2013), a Python implementation of the Affine Invariant MCMC Ensemble sampler (Goodman & Weare 2010). We seed 60 MCMC walkers with initial values widely spread in the prior parameter space. For convergence, we ensure that the chains for all parameters are well-mixed as indicated by Gelman–Rubin metrics smaller than 1.02 (Gelman & Rubin 1992). After an initial burn-in phase, we generally find good convergence after 3000–4000 iterations for each of the 60 walkers. Since the computational time is not a limiting factor in this work, we quadruple the number of iterations to obtain smooth posterior distributions (Figure 6). The final confidence intervals reported in this work are the 15.87% and 84.13% percentiles of each parameters’ posterior distribution.

3.1.4. Spitzer Results

Our *Spitzer* observations robustly reveal a transit event consistent in transit depth and duration with the super-Earth candidate K2-18b. The transit event, however, occurs approximately 1.85 hr ($7 - \sigma$) before the transit time predicted for K2-18b by Montet et al. (2015), which will be discussed further in the following section.

We also find that, using our new modified PLD systematics model, the final systematics-corrected photometry is near the photon-noise limit and virtually free of red noise and systematics (Figures 2 and 3). All posteriors of *Spitzer*/IRAC systematics parameters are Gaussian-shaped and uncorrelated with the astrophysical parameters in the transit model, indicating that there is no dependency of the astrophysical parameters on the instrument parameters (Figure 6).

3.2. Joint Spitzer/K2 Analysis

To investigate the source of the 7σ discrepancy between the predicted and measured transit times, we perform a global analysis of the *Spitzer* and *K2* data. We directly determine the transit parameters and their uncertainties from the *K2* and *Spitzer* raw photometries by simultaneously fitting the transit light curve model, our *Spitzer*/IRAC instrument model, and linear drifts in the photometry of the *K2* transits. We further assume in this Section 3.2 that K2-18b is orbiting its host star in a Keplerian orbit with a periodic transit ephemeris and that the transit depths at visible wavelength (*K2*) and IR wavelength (*Spitzer*) are identical. These assumptions are relaxed in Sections 3.3 and 3.4 and found to be appropriate.

3.2.1. Instrument Models

Since we fit the *Spitzer* photometry and two *K2* transits simultaneously, our fit now includes 14 free parameters for instrument systematics. As in Section 3.1, we include nine PLD weights and one linear slope to account for the intrapixel sensitivity variations and temporal sensitivity changes in the *Spitzer* photometry (Section 3.1.1). In addition, two free parameters are included for each of the two *K2* transits to account for the linear slope and offset in the *K2* baseline. The log-likelihood function for simultaneously fitting the *Spitzer*

transit and the two *K2* transits is

$$\log L = -\frac{1}{2} \sum_{i=1}^{N_s} \left(\frac{D_{\text{Spitzer}}(t_i) - S(t_i) \cdot f(t_i)}{\sigma_{\text{Spitzer}}} \right)^2 - \frac{1}{2} \sum_{i=1}^{N_1} \left(\frac{D_{\text{K2},1}(t_i) - (m_1 t_i + b_1) \cdot f(t_i)}{\sigma_{\text{K2}}} \right)^2 - \frac{1}{2} \sum_{i=1}^{N_2} \left(\frac{D_{\text{K2},2}(t_i) - (m_2 t_i + b_2) \cdot f(t_i)}{\sigma_{\text{K2}}} \right)^2, \quad (3)$$

where σ_{Spitzer} and σ_{K2} are the fitted photometric scatter values for the *Spitzer* and *K2* photometry, N_s , N_1 , and N_2 are the number of data points for each of the transit light curves, and $m t_i + b$ is the linear baseline for the individual *K2* transit light curves.

3.2.2. Transit Model

Our global light curve fit includes a wavelength-independent planet-to-star radius ratio $p = R_p/R_*$, the impact parameter b , the mid-transit time T_C , and the orbital period P . As in Section 3.1.2, we fix the stellar radius and stellar mass to the values derived based on stellar spectroscopy (Table 2) and assume a circular orbit. For the $4.5 \mu\text{m}$ *Spitzer*/IRAC Channel 2 observations, we use the same quadratic limb darkening profile ($u_1 = 0.007 \pm 0.007$, $u_2 = -0.191 \pm 0.005$) as in Section 3.1.2. For the visible *Kepler* bandpass, we derive the quadratic limb darkening coefficients ourselves using Phoenix models and obtain $u_1 = 0.153 \pm 0.004$ and $u_2 = 0.261 \pm 0.007$.

3.2.3. Spitzer/K2 Results

Our joint analysis of the *Spitzer* and *K2* data reveals that a previously undetected outlier point in the *K2* photometry near the ingress of second *K2* transit is the reason for the 1.85 hr (7σ) discrepancy between the transit time predicted from the *K2* data and the transit time observed by *Spitzer* (Figure 7). Using our newly developed cosmic ray detection algorithm we find that the outlier is caused by a cosmic ray hit near the edge of the target star’s PSF on the detector (Figure 4). After removal of the outlier point, we find that a Keplerian orbit with periodic transit events provides a good joint fit to the *K2* and *Spitzer* transit light curves (Figure 7). Our new best estimate for the transit ephemeris of K2-18b is $T_0 = 2457264.39131^{+0.00060}_{-0.00067}$ and $P = 32.939614^{+0.000101}_{-0.000084}$.

As for the *Spitzer*-only fit in Section 3.1.4, we find that the posteriors of all transit light parameters are Gaussian-shaped and uncorrelated with the parameters in the systematics model. This indicates that the derived astrophysical parameters are independent of the fitted instrument parameters in our joint *Spitzer*/*K2* fit. We further find that including the *K2* in the fit does not compromise the excellent noise characteristic of the fit to the *Spitzer* data (compare Figures 3 and 7(right panel)).

3.3. Individual Transit Times

We perform a second global fit to the *K2* and *Spitzer* data to demonstrate that the initial 1.85 hr discrepancy between the transit time observed by *Spitzer* (Section 3.1) and the expected transit time based on Montet et al. (2015) is well explained by the previously undetected cosmic ray hit in the *K2* data. Our transit timing analysis is identical to the analysis presented in Section 3.2 except that we do not fit for an average orbital

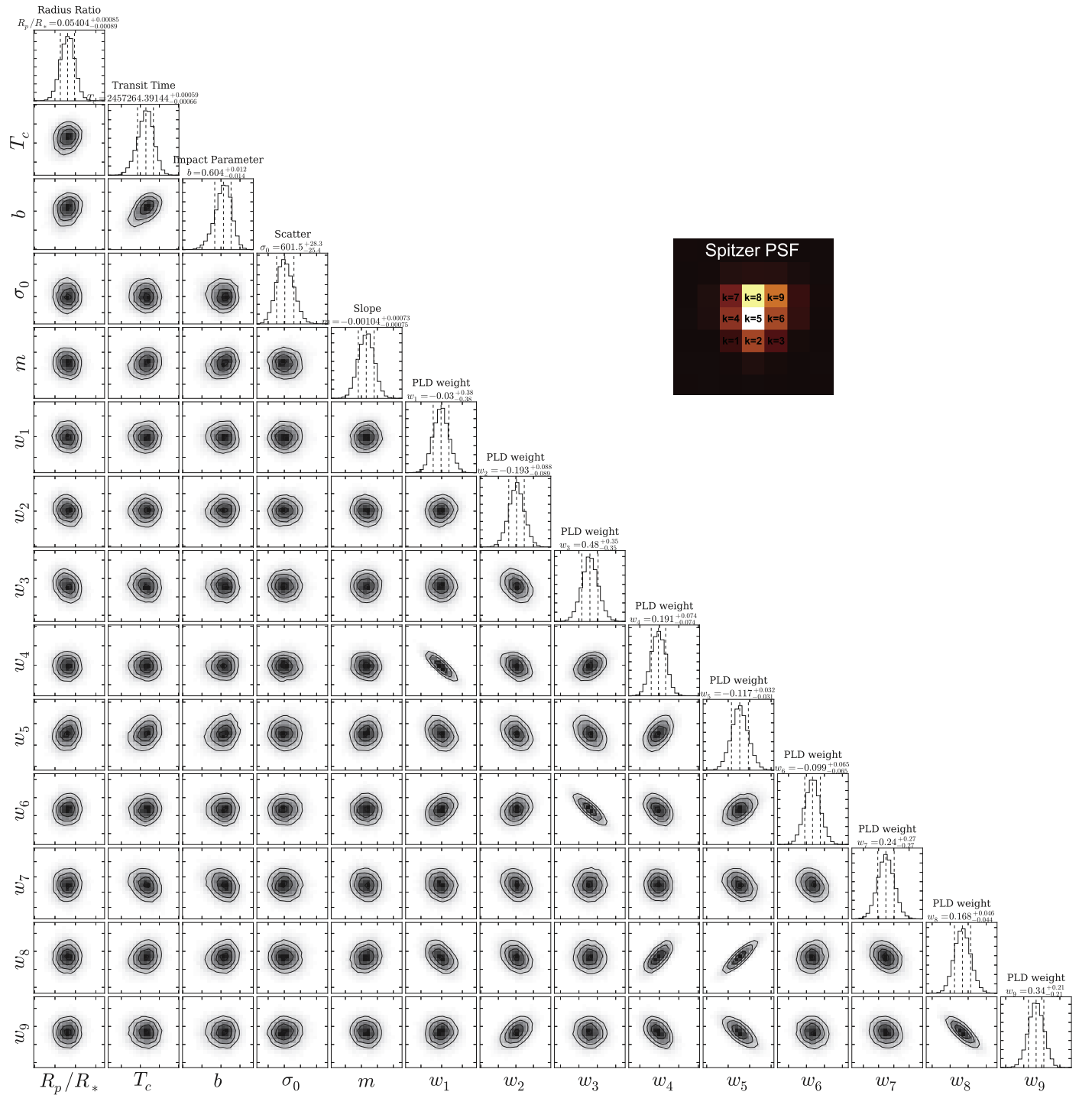


Figure 6. Pairs plot showing the posterior distribution of the MCMC fitting parameters for the *Spitzer* light curve fit. The panels on the diagonal show the marginalized posterior distribution for each fitting parameter. The 68% credible interval is marked by vertical dashed lines and quantified above the panel. The off-diagonal panels show the two-dimensional marginalized distribution for pairs of parameters, with the gray shading corresponding to the probability density and black contours indicating the 68% and 95% credible regions. Our PLD-based *Spitzer* instrument model results in no correlation between astrophysical parameters (R_p/R_* , T_c , b) and instrumental parameters ($w_1 \dots w_9$, m , σ_0). The posterior distribution of all PLD parameters are near-Gaussian. The inset at the top right shows a typical image of K2-18's on the *Spitzer*/IRAC detector, labeling the 3×3 pixels covering the central region of the PSF.

period, but instead parameterize the mid-transit times of all three individual transits individually (Table 1). We remove the discrepant data point near the ingress of the second K2 transit (Figure 7). Finally, we probe for deviations from a linear ephemeris derived in Section 3.2 by plotting the differences between the individually fitted transit times and the calculated

transit times from the best-fitting linear transit ephemeris (Figure 8).

We find that all three measured transit times are fully consistent with a linear ephemeris to within the timing uncertainties of 1–3 minute. We conclude that the K2 and *Spitzer* data are well explained by a single planet in a Keplerian

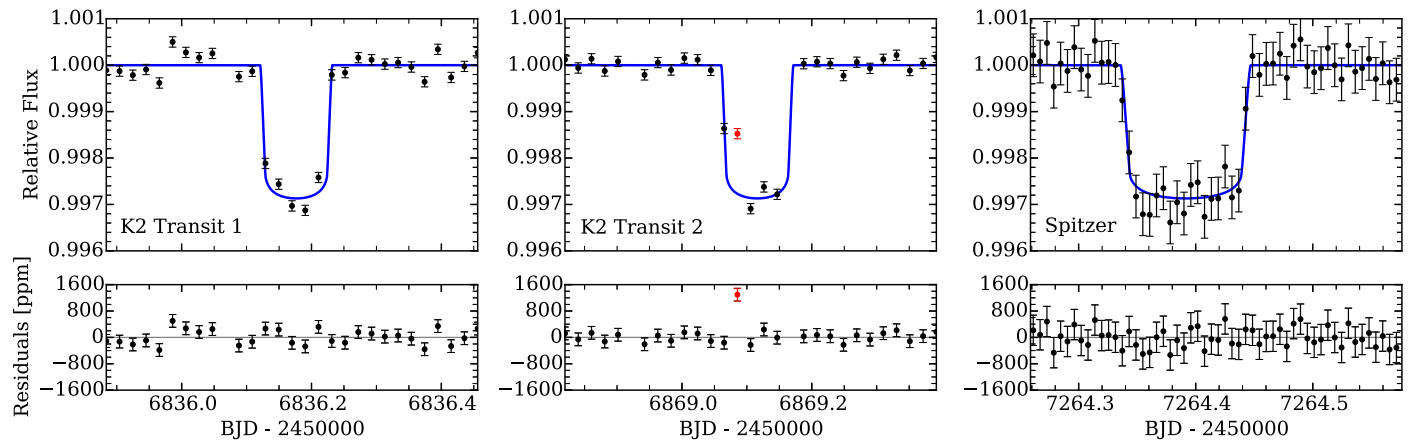


Figure 7. Joint light curve fit to the *K2* and *Spitzer* observation of K2-18b. The top panels show the best fitting model light curve (blue line), overlaid with the systematics-corrected *K2* data (left and middle) and *Spitzer* data (right). Residuals from the light curve fitting are plotted in the bottom panels, with vertical bars corresponding to the fitted photometric scatter. An outlier data point affected by a cosmic ray hit near the ingress of the second *K2* transit is indicated in red and ignored in the light curve fitting (see also Section 2.2.2). The high-cadence *Spitzer* data critically helped in identifying the outlier by precisely constraining the transit duration and transit impact parameter.

Table 1
Transit Parameters Derived from the *Spitzer* and *K2* Light Curves of K2-18b

Parameter	<i>Spitzer</i> Only Keplerian Orbit (Section 3.1)	<i>Spitzer</i> + <i>K2</i> Keplerian Orbit (Section 3.2)	<i>Spitzer</i> + <i>K2</i> Transit Timing (Section 3.3)	<i>Spitzer</i> + <i>K2</i> Transit Depth Comp. (Section 3.4)	Unit
Radius ratio R_p/R_*	$0.05397^{+0.00085}_{-0.00089}$	$0.05295^{+0.00061}_{-0.00059}$	$0.05303^{+0.00059}_{-0.00059}$	$0.05205^{+0.00077}_{-0.00076}$ (<i>Kepler</i>) $0.05391^{+0.00082}_{-0.00088}$ (<i>Spitzer</i>)	1 ...
Impact parameter, b	$0.604^{+0.012}_{-0.014}$	$0.601^{+0.013}_{-0.011}$	$0.603^{+0.011}_{-0.011}$	$0.601^{+0.012}_{-0.011}$	1
<u>Ephemeris:</u>					
Mid-transit time, T_C	$2457264.39144^{+0.00059}_{-0.00066}$	$2457264.39131^{+0.00060}_{-0.00067}$...	$2457264.39135^{+0.00062}_{-0.00066}$	BJD
Orbital period, P	32.94 (fixed)	$32.939614^{+0.000101}_{-0.000084}$...	$32.939622^{+0.000099}_{-0.000094}$	days
<u>Individual transit times:</u>					
<i>K2</i> Transit 1	$2456836.1767^{+0.0008}_{-0.0026}$...	BJD
<i>K2</i> Transit 2	$2456869.11526^{+0.00076}_{-0.00080}$...	BJD
<i>Spitzer</i>	$2457264.39141^{+0.00059}_{-0.00063}$...	BJD

orbit. Future transit observations will be needed to gauge transit timing variations below the 1–3 minute level or with periods several times greater than the 430 days covered by the *K2* and *Spitzer* observations analyzed here.

3.4. Transit Depth Comparison between *K2* and *Spitzer*

We perform a third global analysis of the *K2* and *Spitzer* light curves to compare the transit depths in the visible-light *K2* bandpass (0.4–0.7 μm) and the infrared *Spitzer*/IRAC bandpass (4–5 μm). Widely different transit depths at visible and infrared wavelengths could alert us to the potential presence of a blended star that would affect the inferred planetary radius measurement (Stevenson et al. 2014) or could even be the source of a false positive scenario (Désert et al. 2015). Different transit depths could also result from wavelength-dependent extinction in the atmosphere of K2-18b or the presence of an exosphere or planetary rings.

We perform a global analysis identical to the one described in Section 3.2; however, this time we allow for different transit depths to fit the *K2* and *Spitzer* transit observations (Table 1). We find that the transit depths at visible-light and infrared are consistent to within 1σ uncertainties (Figure 9), ruling out any blended stars or planetary rings that would affect the transit

depth measurement at visible and near-infrared wavelengths by more than 10% (300 ppm). The precision of the transit depth measurements, however, is currently insufficient to detect gravitationally bound atmospheres.

4. DISCUSSION AND CONCLUSIONS

The *Spitzer Space Telescope* observations presented in this work confirm the presence of the habitable zone super-Earth K2-18b by detecting a third transit event with a consistent transit depth near the predicted transit time. The revealed periodicity of the transit signal demonstrates that the two transit-like events observed by *K2* are indeed caused by one planet in a 33 day orbit and are not two independent events caused by two similarly sized planets in >50 day orbits. The periodicity also rules out any scenarios in which one or both of the identified transit-like events were the result of residual systematic effects in the corrected *K2* photometry. The photometric confirmation of K2-18b is critical for future atmospheric studies because K2-18b is an extremely favorable habitable-zone exoplanet for transmission spectroscopy with the *Hubble Space Telescope* (*HST*) and James Webb Space Telescope (*JWST*).

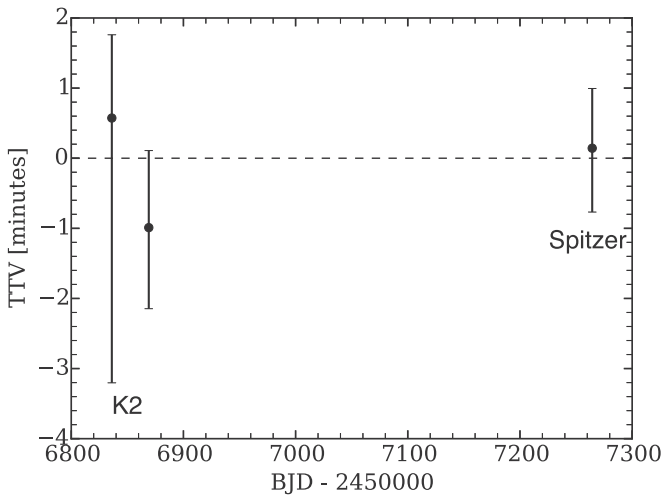


Figure 8. Transit times of K2-18b relative to the best-fitting linear ephemeris extracted from the global fits to the *K2* and *Spitzer* data. After removing the outlier in the *K2* photometry, the data of K2-18b are well explained by a Keplerian orbit with linear ephemeris.

Table 2
Summary of Planet and Host Star Properties

Param	Units	K2-18b
T_0	BJD	$2457264.39144^{+0.00059}_{-0.00066}$
P	d	$32.939614^{+0.000101}_{-0.000084}$
b	...	$0.601^{+0.013}_{-0.011}$
R_p/R_*	%	$5.295^{+0.061}_{-0.059}$
a	au	$0.1429^{+0.0060}_{-0.0065}$
i	degree	$89.5785^{+0.0079}_{-0.0088}$
R_p	R_\oplus	$2.279^{+0.026}_{-0.025}$
S_{inc}	W	1432^{+293}_{-270}
S_{inc}	S_\oplus	$1.05^{+0.22}_{-0.20}$
T_{14}	min	$159.78^{+1.40}_{-1.62}$
T_{23}	min	$135.24^{+1.74}_{-1.96}$
R_*	R_\odot	0.411 ± 0.038
M_*	M_\odot	0.359 ± 0.047
$T_{\text{eff},*}$	K	3457 ± 39
[Fe/H]	(dex)	0.123 ± 0.157
$\rho_{*,\text{spec}}$	g cm^{-3}	7.87 ± 1.26

We also find, however, that the third transit event occurred 1.85 hr ($7 - \sigma$) before the predicted transit time based on the *K2*-derived ephemeris by Foreman-Mackey et al. (2015) and Montet et al. (2015). Our global analysis of the *K2* and *Spitzer* data reveals that this 1.85 hr deviation is, however, not caused by transit timing variations from another planets in the system, but is well-explained by a single, previously undetected cosmic ray hit in the *K2* photometry near the ingress of the second transit.

Our analysis of K2-18b critically reveals that transit ephemerides of long-period planets based on only two detected transit events can strongly be affected by individual outlier data points in the *K2* photometry. A single outlier due to a cosmic ray hit near the ingress of the second transit biased the ephemeris of K2-18b to a level that future transit observations could have missed the transit of K2-18b completely. The deviation in the transit ephemeris would have grown to 8 hr by the time *JWST* launches (Figure 10). As a result, the first transiting habitable-zone planet amenable to

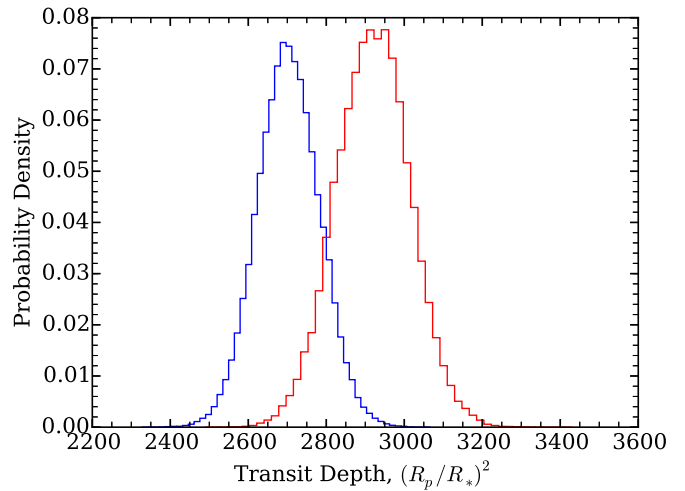


Figure 9. Marginalized posterior distributions of the transit depths in the visible-light *K2* bandpass ($0.4\text{--}0.7\ \mu\text{m}$, blue) and in the infrared *Spitzer*/IRAC Channel 2 bandpass ($4\text{--}5\ \mu\text{m}$, red). The fitted transit depths from the *Spitzer* and *K2* data are consistent to within approximately $1 - \sigma$.

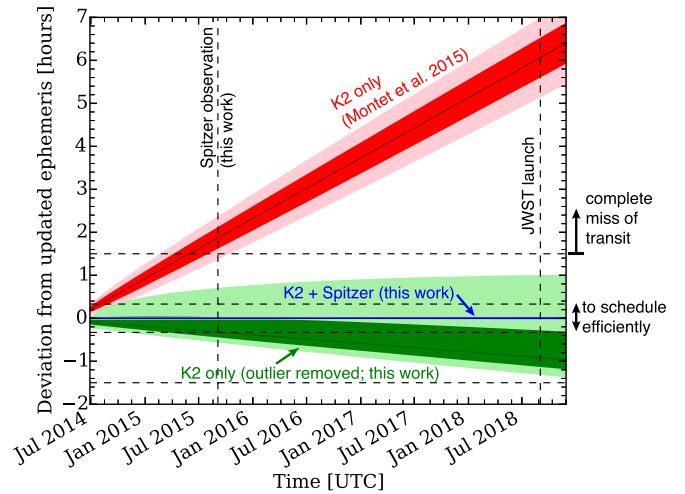


Figure 10. Deviations from the updated ephemeris. The red region illustrates the deviation in the predicted mid-transit time between the *K2*-derived ephemeris reported by Montet et al. (2015) and our updated ephemeris based on the joint *K2*-*Spitzer* analysis (blue). Dark and light red regions correspond to 68% and 95% confidence, respectively. Equivalently the blue regions (within the line thickness) correspond to the uncertainties of the updated *K2*-*Spitzer* ephemeris. Without the immediate *Spitzer* follow-up, K2-18b would have been for lost for future atmospheric characterization due to the increasing deviation in the predicted transit time. For comparison, the green region indicates the transit timing uncertainty by refitting only the *K2* data without the outlier data point. The ephemeris based on only *K2* remains uncertain to 1–2 hr, but the bias is eliminated by removing the outlier.

efficient atmospheric characterization would have been lost for future spectroscopic transit observations with *HST* or *JWST* due to the increasing error in its ephemeris estimate. We conclude that immediate follow-up of prime exoplanet candidates is critical for long-period planets found by planet search missions such as *K2* and the *Transiting Exoplanet Survey Satellite (TESS)*.

Similarly, the previously undetected outlier in the *K2* photometry introduced substantial uncertainty in the inference of the planet-to-star radius ratio. After identifying the cosmic ray hit and removing the outlier we estimate the planet-to-star radius ratio to $R_p/R_* = 5.295\%^{+0.061\%}_{-0.059\%}$. If we ignore our

knowledge about the cosmic ray hit and include the outlier data point in our analysis of the *K2* light curve, we find the radius ratio uncertainty to be nine times larger, consistent with $5.13\%_{-0.35\%}^{+0.56\%}$ as reported by Foreman-Mackey et al. (2015). In this latter case, the wide and asymmetric uncertainties arise because the outlier data point adversely affects the overall fit to the low-cadence *K2* photometry. We present an efficient search algorithm to identify cosmic ray hits in photometry data sets with substantial telescope pointing jitter to avoid similar problems in future *K2* or *TESS* light curve analyses.

In the coming years, mass measurement of K2-18b will be critical to provide an understanding of the nature and bulk composition of K2-18b. Radial velocity measurements are challenging, however, because the host star is faint at visible wavelengths ($V = 13.5$) and the expected radial velocity semi-amplitude is small ($K_p = 1\text{--}2\text{ m s}^{-1}$). Still, thanks to the star's brightness in the near-infrared ($K = 8.9$), K2-18b may present an ideal target for intensive follow-up with a number of upcoming near-infrared radial velocity instrument such as CARMENES (Quirrenbach et al. 2012), SPIRou (Artigau et al. 2014), IRD (Tamura et al. 2012), and CRILES (Kaeuffl et al. 2004). In addition, upcoming visible-light radial velocity instruments on large telescopes like VLT/ESPRESSO (Pepe et al. 2014), Keck/SHREK, and GMT/G-CLEF (Szentgyorgyi et al. 2012) should also be able to measure the planetary mass of K2-18b in the coming years.

The IR brightness and small stellar radius of the host star make K2-18b an extremely favorable candidate for the first detailed atmospheric characterization of a habitable-zone super-Earth. Given its radius of $2.27R_{\oplus}$, the planet is likely surrounded by a thick gaseous envelope (e.g., Rogers 2015) that could be amenable to characterization through transit spectroscopy. Eventually the detectability of K2-18b's atmosphere will depend on the mean molecular mass of the atmosphere and presence of high-altitude clouds (Miller-Ricci et al. 2009; Benneke & Seager 2013). In addition, the range of plausible atmospheric scenarios for K2-18b also depends on the as yet unknown planetary mass and surface gravity. Little is known about the nature of planets in the habitable zone around M stars, making K2-18b a unique opportunity to probe chemical composition and formation history with future follow-up observations.

The *K2* and *Spitzer* analyses presented in this work were performed using ExoTEP, a newly developed, Python-based light curve analysis framework. The new framework is highly modular in that it can jointly fit any number of *Kepler*, *Spitzer*, *HST*/WFC3, and/or *HST*/STIS transit observations in a global Markov chain Monte Carlo analysis with minimum user input. In this work, the joint analysis of *Spitzer* and *K2* data provides substantial advantage over individual transit fits because the high cadence *Spitzer* observations provide exquisite constraints on the transit duration, which helps fitting the low-cadence *K2* data. For the analysis of the *Spitzer* observations, we introduce two modifications to the PLD approach introduced by Deming et al. (2015). We find that these changes can provide substantial advantages in the convergence and uncertainty estimation. With the modifications, the posterior distribution of all PLD weights in our analyses converge to Gaussian-shaped posteriors that are uncorrelated with the astrophysical parameters, providing confidence that the derived transit light curve parameters are independent of the instrument parameters. Critically, our corrected *Spitzer* light curve is virtually free of

residual red noise or systematics. The photometric precision of our final *Spitzer* light curve is near the Poisson limit.

This work is based in part on observations made with the *Spitzer Space Telescope*, which is operated by the Jet Propulsion Laboratory, California Institute of Technology under a contract with NASA. Support for this work was provided by NASA through grants under the HST-GO-13665 program from the STScI and through an award issued by JPL/Caltech. AWH acknowledges support for our *K2* team through a NASA Astrophysics Data Analysis Program grant. AWH and IJM acknowledge support from the *K2* Guest Observer Program. H.A.K. acknowledges support from the Sloan Foundation.

Facilities: *Spitzer*, *Kepler*, *K2*, IRTF (SpeX).

REFERENCES

- Artigau, É., Kouach, D., Donati, J.-F., et al. 2014, *Proc. SPIE*, 9147, 914715
 Beichman, C., Livingston, J., Werner, M., et al. 2016, *ApJ*, 822, 39
 Benneke, B., & Seager, S. 2013, *ApJ*, 778, 153
 Boyajian, T. S., von Braun, K., van Belle, G., et al. 2012, *ApJ*, 757, 112
 Burke, C. J., Christiansen, J. L., Mullally, F., et al. 2015, *ApJ*, 809, 8
 Claret, A., & Bloemen, S. 2011, *A&A*, 529, A75
 Crossfield, I. J. M., Petigura, E., Schlieder, J. E., et al. 2015, *ApJ*, 804, 10
 Cushing, M. C., Rayner, J. T., & Vacca, W. D. 2005, *ApJ*, 623, 1115
 Deming, D., Knutson, H., Kammer, J., et al. 2015, *ApJ*, 805, 132
 Désert, J.-M., Charbonneau, D., Torres, G., et al. 2015, *ApJ*, 804, 59
 Farr, W. M., Gair, J. R., Mandel, I., & Cutler, C. 2015, *PhRvD*, 91, 023005
 Foreman-Mackey, D., Hogg, D. W., Lang, D., & Goodman, J. 2013, *PASP*, 125, 306
 Foreman-Mackey, D., Hogg, D. W., & Morton, T. D. 2014, *ApJ*, 795, 64
 Foreman-Mackey, D., Montet, B. T., Hogg, D. W., et al. 2015, *ApJ*, 806, 215
 Gelman, A., & Rubin, D. B. 1992, *StatSci*, 7, 457
 Gilliland, R. L., Jenkins, J. M., Borucki, W. J., et al. 2010, *ApJL*, 713, L160
 Goodman, J., & Weare, J. 2010, *Communications in Applied Mathematics and Computational Science*, 5, 65
 Grillmair, C. J., Carey, S. J., Stauffer, J. R., et al. 2012, *Proc. SPIE*, 8448, 1
 Hauschildt, P. H., Allard, F., & Baron, E. 1999, *ApJ*, 512, 377
 Ingalls, J. G., Krick, J. E., Carey, S. J., et al. 2012, *Proc. SPIE*, 84421, 1
 Kaeuffl, H.-U., Ballester, P., Biereichel, P., et al. 2004, *Proc. SPIE*, 5492, 1218
 Kammer, J. A., Knutson, H. A., Line, M. R., et al. 2015, *ApJ*, 810, 118
 Knutson, H. A., Lewis, N., Fortney, J. J., et al. 2012, *ApJ*, 754, 22
 Kreidberg, L. 2015
 Lépine, S., Hilton, E. J., Mann, A. W., et al. 2013, *AJ*, 145, 102
 Lewis, N. K., et al. 2013, *ApJ*, 766, 95
 Mandel, K., & Agol, E. 2002, *ApJL*, 580, L171
 Mann, A. W., Brewer, J. M., Gaidos, E., Lépine, S., & Hilton, E. J. 2013a, *AJ*, 145, 52
 Mann, A. W., Feiden, G. A., Gaidos, E., Boyajian, T., & Braun, K. v. 2015, *ApJ*, 804, 64
 Mann, A. W., Gaidos, E., & Ansdell, M. 2013b, *ApJ*, 779, 188
 Mighell, K. J. 2005, *MNRAS*, 361, 861
 Miller-Ricci, E., Seager, S., & Sasselov, D. 2009, *ApJ*, 690, 1056
 Montet, B. T., Morton, T. D., Foreman-Mackey, D., et al. 2015, *ApJ*, 809, 25
 Pepe, F., Molaro, P., Cristiani, S., et al. 2014, *AN*, 335, 8
 Petigura, E. A., Marcy, G. W., & Howard, A. W. 2013, *ApJ*, 770, 69
 Petigura, E. A., Schlieder, J. E., Crossfield, I. J. M., et al. 2015, *ApJ*, 811, 102
 Quirrenbach, A., Amado, P. J., Seifert, W., et al. 2012, *Proc. SPIE*, 8846, 88460
 Rayner, J. T., Cushing, M. C., & Vacca, W. D. 2009, *ApJS*, 185, 289
 Rogers, L. A. 2015, *ApJ*, 801, 41
 Rojas-Ayala, B., Covey, K. R., Muirhead, P. S., & Lloyd, J. P. 2012, *ApJ*, 748, 93
 Schlieder, J. E., Crossfield, I. J. M., Petigura, E. A., et al. 2016, *ApJ*, 818, 87
 Silburt, A., Gaidos, E., & Wu, Y. 2015, *ApJ*, 799, 180
 Stevenson, K. B., Bean, J. L., Madhusudhan, N., & Harrington, J. 2014, *ApJ*, 791, 36
 Szentgyorgyi, A., Frebel, A., Furesz, G., et al. 2012, *Proc. SPIE*, 8846, 88461
 Tamura, M., Suto, H., Nishikawa, J., et al. 2012, *Proc. SPIE*, 8446, 84461T
 Todorov, K. O., Deming, D., Knutson, H. A., et al. 2013, *ApJ*, 770, 102
 Vanderburg, A., & Johnson, J. A. 2014, *PASP*, 126, 948